AGU PUBLICATIONS

JGR

Journal of Geophysical Research: Atmospheres

RESEARCH ARTICLE
10.1002/2016JD025376

Key Points:
- Annual averaged cloud parameters agree well with TRMM precipitation and derived currents
- Cloud parameters can be used to derive Wilson currents in a global climate model
- Derived Wilson currents show a similar diurnal variation as that seen in past climatological variations

Correspondence to:
C. Kalb,
kalb@address.edu

Citation:
Kalb, C., W. Deierling, A. Baumgaertner, M. Peterson, C. Liu, and D. Mach (2016), Parameterizing total storm conduction currents in the Community Earth System Model, *J. Geophys. Res. Atmos.*, *121*, 13,715–13,734, doi:10.1002/2016JD025376.

Received 17 MAY 2016
Accepted 31 OCT 2016
Accepted article online 2 NOV 2016
Published online 28 NOV 2016

Parameterizing total storm conduction currents in the Community Earth System Model

Christina Kalb[1], Wiebke Deierling[2], Andreas Baumgaertner[2], Michael Peterson[1], Chuntao Liu[3], and Douglas Mach[4]

[1]National Center for Atmospheric Research, Boulder, Colorado, USA, [2]Department of Aerospace Engineering, University of Colorado Boulder, Boulder, Colorado, USA, [3]Texas A&M University–Corpus Christi, Corpus Christi, Texas, USA, [4]Universities Space Research Association, Huntsville, Alabama, USA

Abstract Electrified clouds are known to play a major role in the Global Electric Circuit. These clouds produce upward currents which maintain the potential difference between Earth's surface and the upper atmosphere. In this study, model output from two simulations of the Community Earth System Model (CESM) are compared with conduction currents and other data derived from the Tropical Rainfall Measuring Mission (TRMM) satellite, including both the Lightning Imaging Sensor and Precipitation Radar. The intention is to determine CESM's skill at representing these microphysical and dynamical properties of clouds. Then, these cloud properties are used to develop a model parameterization to compute conduction currents from electrified clouds. Specifically, we evaluate the ability of global mean convective mass flux, ice water path, and convective precipitation to represent conduction current sources. Parameterizations using these variables yield derived global mean currents that agree well with the geographical patterns of TRMM currents. In addition, comparing the diurnal variations of modeled global mean current to the observed diurnal variations of electric potential gradient, root-mean-square (RMS) errors range between 6.5% and 8.1%, but the maximum occurs 4 to 6 h early in all three variables. Output currents derived from the model variables generally match well to the currents derived from TRMM, and the total global current estimates agree well with past studies. This suggests that cloud parameters are well suited for representing the global distribution and strength of currents in a global model framework.

1. Introduction

An electric field exists between Earth's surface and the ionosphere, with a quasi-static potential of about 240 kV. Electrified clouds play an important role in maintaining this potential difference [*Wilson*, 1920; *Whipple*, 1929]. These clouds produce an upward conduction current (referred to as a Wilson current) from the top of the cloud to the ionosphere that is the primary current source to the global electric circuit [*Bering et al*., 1998; *Mach et al*., 2011]. However, not all clouds contribute equally, and the exact contribution from different types of clouds is not entirely known at this time [*Williams and Mareev*, 2014].

Cloud electrification has been researched extensively in the last century. Several mechanisms responsible for electrifying clouds have been proposed and investigated, including precipitation based charging mechanisms, ion capture mechanisms, and melting-related mechanisms in anvils and stratiform regions [*Dye and Willett*, 2007; *Kuhlman et al*., 2009; *Stolzenburg et al*., 1994]. Although multiple mechanisms contribute to cloud electrification, the noninductive charging mechanism is thought to play the dominant role in thunderstorm electrification [*Latham*, 1981; *Jayaratne et al*., 1983; *Keith and Saunders*, 1989; *MacGorman and Rust*, 1998]. In this mechanism, rimed hydrometeors collide with ice crystals, resulting in a net opposite charge on each species of ice hydrometeors. Through gravitational sorting, the heavier rimed hydrometers collect mostly in the lower portion of the cloud while the ice crystals are transported to the upper parts of the cloud, creating net negative and positive charge regions. The magnitude of charge transfer depends on temperature, liquid water content, size of the ice crystals, and other factors [*Saunders and Peck*, 1998; *Takahashi and Miyawaki*, 2002].

In support of the noninductive charging mechanism, multiple observational studies, including studies based on radar observations, have shown strong relationships between updraft strength, parameters characterizing the mixed phase microphysics (between 0°C and −40°C), and storm electrification resulting in lightning. For example, *Deierling et al*. [2008] examined the relationship between precipitation ice mass fluxes for

temperatures colder than −5°C and lightning frequency for storms over Northern Colorado/Kansas and Northern Alabama. They found a good correlation between precipitation and nonprecipitation ice mass as well as their fluxes and total lightning flash rate. Based on Tropical Rainfall Measuring Mission (TRMM) Precipitation Radar (PR) and Lightning Imaging Sensor (LIS) data from 1998 to 2000, *Petersen et al*. [2005] found that radar-derived ice water path, defined as the integration of ice water content above −10°C, was highly correlated with lightning flash density in the tropics and subtropics. *Liu et al*. [2012] used 13 years of TRMM PR data and examined multiple radar-based variables in relation to LIS lightning data. They found high correlations between lightning flash rates and radar reflectivities greater than 30, 35, and 40 dBZ between 0°C and −40°C. They also noted that these relationships varied between oceanic and continental storms.

Several studies have also examined the relationship between storm updrafts and lightning characteristics. *Wiens et al*. [2005] examined one supercell in northern Colorado and found that total lightning flash rates correlated well with the volume of updraft speeds greater than 10 m s^{-1}. *Deierling and Petersen* [2008] examined storms over Northern Colorado, Kansas, and Alabama. They found the best correlations between updraft volume for temperatures colder than −5 and −10°C with vertical velocities greater than 5 and 10 m s^{-1} and total lightning flash rates.

Recent studies have also shown a correlation between electrical activity and storm Wilson currents. *Davydenko et al*. [2009] modeled two thunderstorms, one over New Mexico and another over Oklahoma, and compared the modeled electric field profiles with the observations described in *Stolzenburg et al*. [1998, 2002]. The model produced reasonable estimates of the measured electric fields and showed that the Oklahoma storm had a higher flash rate, larger average updraft speed, and also produced a larger Wilson current than the less active New Mexico storm. Furthermore, *Mach et al*. [2010] examined electric field data for 850 overflights of electrified clouds. They found that storms with lightning, on average, produced larger Wilson currents than those without lightning. These studies suggest that storm microphysical and dynamical properties may potentially represent conduction currents well.

A comprehensive model of the global electric circuit (GEC), including the representation of storm conduction currents based on dynamical and microphysical properties of electrified clouds has not yet been developed. However, past and recent studies have incorporated parameterizations for lightning in global models. These studies include *Price and Rind* [1992, 1994], *Allen and Pickering* [2002], and *Tost et al*. [2007]. Additionally, *Kalinin et al*. [2011] developed an approach to calculate the contributions of different cloud types to the GEC based on model-derived convective areas. Applying this approach, *Mareev and Volodin* [2014] represented the contribution of thunderstorms and electrified shower clouds to the ionospheric potential using an exponential conductivity profile in a climate model. They performed a 120 year simulation to examine the diurnal and seasonal variation in the ionospheric potential. Our study differs from the above, in that we use cloud properties to estimate conduction currents rather than lightning flash rates or contributions to the ionospheric potential. The resulting parameterization can be used as part of an evolving physics-based GEC global modeling framework that includes conductivity, source currents, and external influences from the magnetosphere to the global electric circuit, such as that in *Baumgaertner et al*. [2014] and *Lucas et al*. [2015].

To simulate the contribution of currents from different electrified clouds to the GEC, this study develops a model parameterization specifically for the Community Earth System Model (CESM), based on the skill of relevant cloud parameters in representing currents. Details of the CESM model and observational data sets are given in section 2. Then, in section 3, CESM model precipitation is compared with precipitation data from the TRMM satellite to evaluate the model timing, intensity, and potential model biases or deficiencies. In section 4, CESM's microphysical and dynamical properties of storms are used in conjunction with a TRMM-based current map to investigate relationships for total storm currents. A parameterization of currents within CESM is then derived from these relationships. In section 5, the results from this parameterization are discussed and section 6 summarizes the CESM conduction current parameterization and simulations results.

2. Model and Observations

2.1. CESM Model

CESM [*Neale et al*., 2013] is a fully coupled community global climate model maintained by the National Center for Atmospheric Research (NCAR). The atmospheric component of CESM, the Community

Atmosphere Model (CAM), includes the relevant dynamical, physical, and chemical processes of the troposphere and stratosphere on horizontal scales of 10 to 300 km.

In this study, we show results from two different CESM simulations over the course of 1 year (2005): a free-running simulation with CAM5 physics (free), and a simulation nudged with GEOS-5 reanalysis data (nudged). Both simulation use CESM model version 1.2.2 and were initialized with present-day conditions (the time options in CESM are preindustrial, present day, and future). The resolution of the atmospheric model component is approximately 25 km.

Nudging, also called Newtonian relaxation, is a simple form of data assimilation. Additional terms are added to the equations for temperature, horizontal wind, and specific humidity, which nudge them toward the observed values at every time step. The nudging terms in CAM are the same for all variables. An example of the nudging term for temperature is given in equation (1), where T_m is the modeled temperature, T_r is the reanalysis temperature, and τ is the relaxation time.

$$\text{nudged\_terms} = \frac{T_m - T_r}{\tau} \tag{1}$$

Cloud physics in CAM as well as the convective schemes employed are particularly relevant for this study. For deep convection, the Zhang-McFarlane scheme is used [*Zhang and McFarlane*, 1995]. However, this scheme is modified by adding convective momentum transport according to *Richter and Rasch* [2008] and a modified dilute plume calculation following *Raymond and Blyth* [1986, 1992]. The Zhang-McFarlane convection scheme is based on a plume ensemble approach where it is assumed that an ensemble of convective scale updrafts (and the associated saturated downdrafts) may exist whenever the atmosphere is conditionally unstable in the lower troposphere. The updraft ensemble is composed of plumes sufficiently buoyant so as to penetrate the unstable layer, where all plumes have the same upward mass flux at the bottom of the convective layer.

Moist convection occurs only when there is Convective Available Potential Energy (CAPE) for which parcel ascent from the subcloud layer acts to release CAPE at an exponential rate using a specified adjustment time scale. For evaporation of convective precipitation on its way to the surface, the scheme by *Sundqvist* [1988] is used. This scheme relates the rate at which raindrops evaporate to the local large-scale subsaturation and the rate at which convective rainwater is made available to the subsaturated model layer.

The role of the shallow convection scheme is to vertically transport heat, moisture, momentum, and tracers by asymmetric turbulences. In the model, the shallow convection scheme is performed after the deep convection scheme, where the cloud top height and the existence of convective precipitation and convective downdraft set the two schemes apart. The shallow convection scheme does not have any limitation on its cloud top height and convective precipitation, but since the preceding deep convection scheme consumes most CAPE and stabilizes the atmosphere, cloud top height is naturally limited. The scheme assumes a steady state convective updraft plume, and a small updraft fractional area, so that compensating subsidence entirely exists within the same grid box as the convective updraft.

The microphysics scheme is a two-moment scheme based on *Morrison et al*. [2005] and predicts the number concentrations and mixing ratios of cloud droplets, cloud ice, snow, and rain. The size distributions are represented by gamma functions and assume spherical particles. Subgrid cloud variability is treated for cloud water to be able to derive grid average microphysical process rates. Precipitation is treated diagnostically. For more details on the convective and microphysics/macrophysics schemes see *Neale et al*. [2010, and references therein].

Various CESM model output parameters which represent the updraft and mixed phase characteristics associated with cloud electrification were identified and include convective mass flux, in cloud ice water path, and convective precipitation. The net vertical convective mass flux is the total of both the upward and downward components. The upward convective mass flux is defined as

$$M_u = M_b \frac{e^{\lambda D(z-z_b)} - 1}{\lambda_0 (z - z_b)} \tag{2}$$

where M_b is the cloud base convective mass flux, λ_0 is the maximum detrainment rate for the updraft plume that is detraining at height z_0, and λ_D is the entrainment rate for the updraft which detrains at height z. The downward component has a similar form to equation (2), but also includes a factor to ensure that the

downdraft strength is consistent with precipitation availability. Ice water path is defined as the integral of the prognostic ice water, in mass per unit area (A. Gettelman, personal communication, 2016). The prognostic ice water is from the cloud microphysics scheme [*Morrison and Gettelman*, 2008], with prognostic ice generated by the cloud condensation scheme [*Park et al*., 2014]. The cloud condensation scheme also takes detrained condensate from convection and speciates it into liquid and ice based on a temperature ramp [*Neale et al*., 2010]. Since the noninductive charging mechanism is more efficient when supercooled liquid water is present, in-cloud ice water path and convective mass flux were integrated between 0°C and −50°C. These variables may potentially be able to represent cloud conduction currents.

2.2. TRMM Precipitation

To evaluate the model simulations, particularly the model representation of convective clouds, rainfall rates from the precipitation radar (PR) onboard the TRMM satellite [*Kummerow et al*., 1998] were compared to modeled rainfall rates. The PR measures radar reflectivity factor at 13.8 GHz over a swath of 220 km with a vertical resolution of 250 m at nadir. Rainfall rates are calculated using a power law in the form of $R = aZ^b$, where a and b are functions of the rain type (stratiform and convective), heights of the 0°C isotherm, and storm top.

For this paper, the TRMM 3A25 [*Meneghini et al*., 2001] 0.5° gridded monthly PR data from the surface level, defined as the lowest level of detected radar reflectivity, were used. Also, the given rain rates were multiplied by the fraction of nonzero pixels to account for the fact that an entire grid box of TRMM data may not be raining. The TRMM data were also corrected for the effects of the orbit boost in August 2001 by adjusting the rainfall rates after this time by 5.9%, following *Shimizu et al*. [2009].

2.3. Derived Conduction Currents

In addition to the TRMM PR data, CESM output was also compared to total storm conduction current climatologies derived from two specific sources. The first is a precipitation and cloud feature database in *Liu et al*. [2008]. This database contains counts of thunderstorms and electrified shower clouds (ESCs) in 1° × 1° grid boxes between 35° south and 35° north latitude, over a 13 year period (1998–2010). The counts of thunderstorms and electrified shower clouds give climatological means for a monthly composite day. In this study, the storm areas are not considered.

Conduction currents were calculated from the above database using mean currents from 850 aircraft overflights for thunderstorms and ESCs over oceans and land (Figure 1) from *Mach et al*. [2010]. These data emerge from many NASA ER-2 [*Heymsfield et al*., 2001] and ALTUS [*Mach et al*., 2005] overflight measurements of oceanic and continental clouds in the Western Pacific, North America, Caribbean, and Brazil. Specifically, the database contains electric field components measured from 2, 6, 7, or 8 rotating vane electric field mills [*Bateman et al*., 2007] and conductivity from Gerdien capacitor conductivity probes [*Mitchell et al*., 1990; *Bailey et al*., 1999].

The currents were computed from peak-smoothed vertical electric field data where contributions due to lightning were removed. In addition, in some cases the aircraft was unable to fly directly over the center of the storm. For those cases, the peak over the storm center was estimated by taking into account the wing to wing horizontal component of the electric field. Full details on converting the electric field measurements to currents can be found in *Mach et al*. [2009].

Using the *Liu et al*. [2008] database, currents were first estimated by multiplying the *Mach et al*. [2010] mean current values of 1.7 A for thunderstorms and 0.41 A for ESCs with the counts of thunderstorms and ESCs over oceans from *Liu et al*. [2010]. Also, the mean current values of 1.0 A and 0.13 A were multiplied with the thunderstorm and ESC counts over land. This methodology produced a total current estimate of 1609 A for the region between 35° north and south. The indicated value is more akin to the global current estimate of 1400 A [*Kraakevik*, 1961], yet it covers only the tropical and subtropical latitudes.

One concern with the aircraft data is that we have a limited data set covering only a few locations, and thus it may be potentially biased by a few large values. To examine the sensitivity of the estimated global total current, two methodologies were investigated. The first was using the median of each data set, which gives values of 0.85 A and 0.16 A over oceans for thunderstorms and ESCs, respectively. Over land, the median values are 0.38 A and 0.05 A. The median values give a topical total of 618 A.

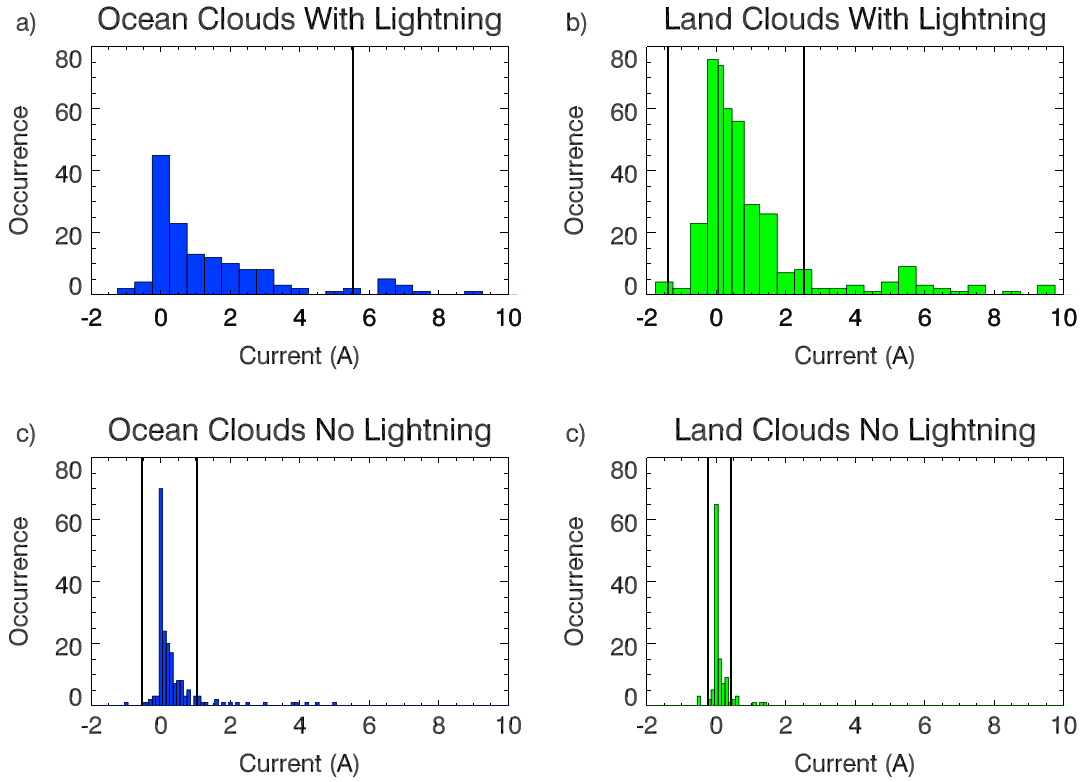

Figure 1. The distribution of currents derived from 850 overflights of the ER-2 aircraft (data from *Mach et al.* [2010]) for (a) ocean clouds with lightning, (b) land clouds with lightning, (c) ocean clouds without lightning, and (d) land clouds without lightning. The black lines show the boundaries for rare events.

The second method was to compute a new mean excluding rare events with large currents by applying the following criteria from *Moore and McCabe* [1999]:

$$\text{exclude}_{\text{high}} = Q3 + 1.5 \times \text{IQR} \quad (3)$$

$$\text{exclude}_{\text{low}} = Q1 - 1.5 \times \text{IQR} \quad (4)$$

where $Q1$ and $Q3$ are the first and third quartiles of data and $\text{IQR} = Q3 - Q1$. Rare events identified using these equations amount to 84 out of the total 850 overflights, slightly less than 10% of the data and are shown by the black vertical lines in Figure 1. The new means computed with rare events removed yield values of 1.17 A and 0.48 A for thunderstorms and ESCs over oceans, and 0.21 A and 0.08 A over land. Using these mean current values results in a total current of 867 A for the tropical regions. In *Cecil et al.* [2014], the measured flash rate over the TRMM domain was found to comprise approximately 90% of the global lightning. Using the previous global total measurement of 1400 A [*Kraakevik*, 1961], the 867 A computed from the mean with rare events removed is closer to comprising 90% of the global total than the 618 A found using the median. Therefore, the new mean current values were selected for this study.

Model- and observational-derived currents were divided based on geographic location for several reasons. First, studies have shown regional differences in relationships between lightning flash rate and cloud ice characteristic distributions [*Boccippio et al.*, 2000; *Mach et al.*, 2007, 2010; *Liu et al.*, 2012]. In particular, global lightning observations have indicated that lightning is most frequent over land and can be absent from large deep convective systems over the oceans [*Christian et al.*, 2003; *Cecil et al.*, 2005; *Liu et al.*, 2010]. This may be due to the weaker vertical velocities seen in convective updrafts over the ocean [*LeMone and Zipser*, 1980; *Zipser and LeMone*, 1980; *Zipser*, 1994] which would result in fewer large ice particles with oceanic storms [*Zipser and Lutz*, 1994]. Having these large ice particles at high elevations is important for charge separation and lightning initiation [*Rutledge and Petersen*, 1994; *Lang et al.*, 2000; *Liu et al.*, 2012]. Therefore, it may be the case that there are different current distributions for land and ocean convection.

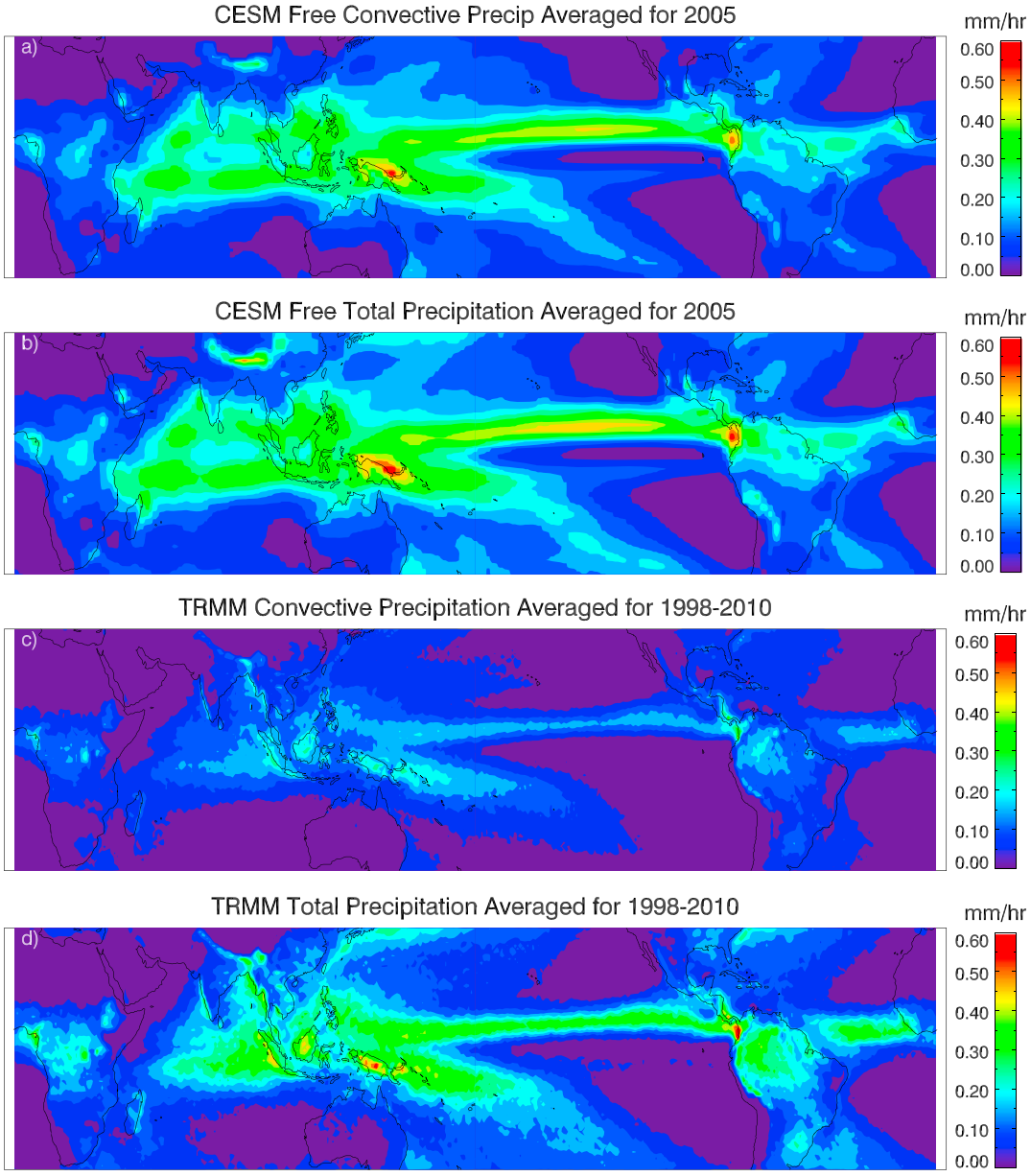

Figure 2. A comparison of the CESM precipitation averaged over 2005 with observed TRMM precipitation averaged across 1998–2010. The specific fields are (a) convective precipitation from the CESM free-running simulation, (b) total precipitation from the CESM free-running simulation, (c) convective precipitation from TRMM, and (d) total precipitation from TRMM.

For the above reasons, each grid box was classified as either land or ocean. Land grid boxes were defined as having greater than 10% land mass and ocean less than 10% land mass. The model data were averaged across 2005 and verified by comparing them directly to the TRMM precipitation data. Then, the model was compared to the derived current data.

3. Evaluation of CESM Precipitation and Microphysics Parameters

3.1. TRMM Precipitation Validation

Figure 2 shows a comparison of CESM free-running convective precipitation to the TRMM convective and total precipitation spanning the same years as the derived currents, 1998 to 2010. For both simulations,

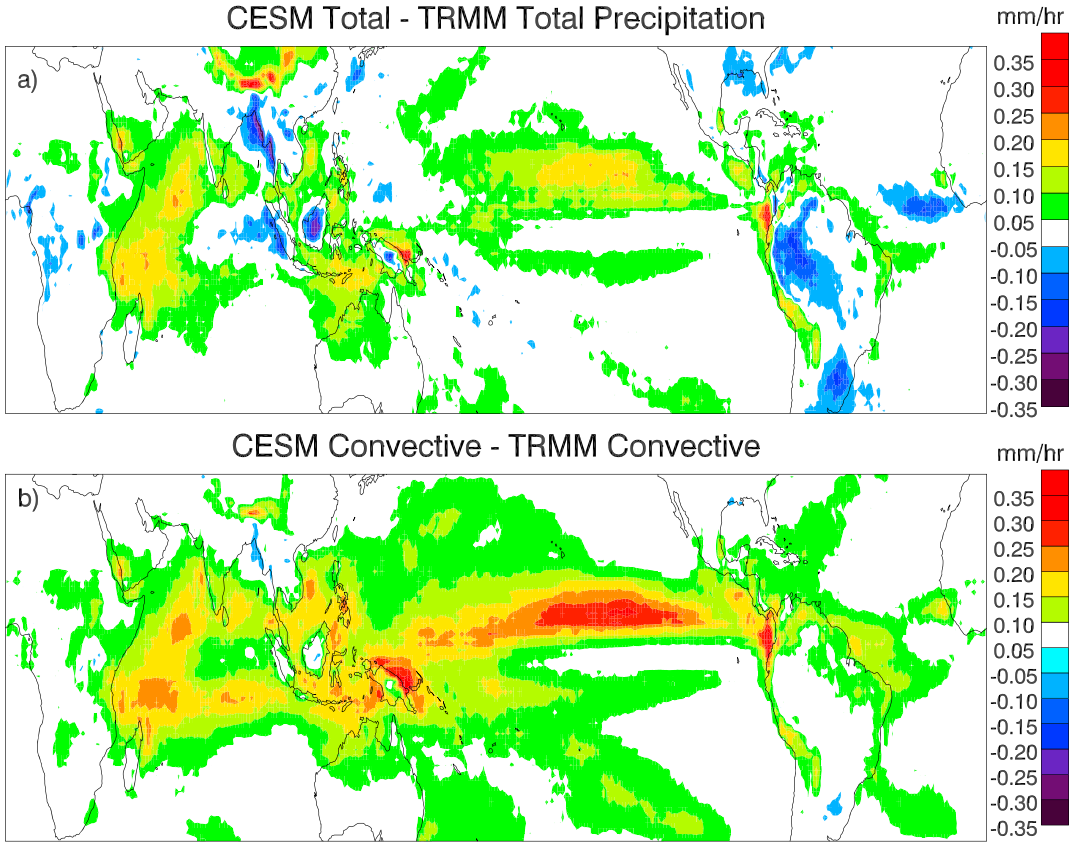

Figure 3. A comparison of the difference between the free-running CESM precipitation rate versus the TRMM precipitation rate for (a) total precipitation and (b) convective precipitation.

CESM convective precipitation rates match the TRMM total precipitation rates more closely, with correlation coefficients of 0.83 for the free-running simulation and 0.85 for the nudged version. This is consistent with the findings of *Dai and Trenberth* [2004] who showed that CESM overestimated convective precipitation, with it accounting for over 80% of the total precipitation in the tropics and subtropics. Studies such as *Dai et al.* [1999] and *Trenberth et al.* [2003] suggest that this overestimate of convective precipitation in CESM could be partially a result of the Zhang MacFarlane convective parameterization. Specifically, this scheme does not include convective inhibition, which allows rain to begin earlier (especially over land), limits CAPE values, and thus results in more frequent smaller storms which remove the atmospheric moisture available for stratiform precipitation.

Although the global percentage of convective precipitation is too high, both the free-running and nudged versions of CESM capture the large-scale features seen in TRMM total precipitation, including the Intertropical Convergence Zone (ITCZ) in the Pacific and Atlantic Oceans, and local maxima over Malaysia, Africa, and South America. Two exceptions are the secondary peaks seen off the coast of Asia near Japan and off the coast of North America. These regions are absent in CESM convective precipitation, but do appear in CESM total precipitation (not shown), suggesting that they result from an increased frequency of stratiform precipitation in the midlatitudes.

Figure 3 shows the free-running model minus TRMM difference maps for total precipitation (top) and convective precipitation (bottom). In addition to the features discussed above, some additional information is evident in these maps. First, the model underestimates precipitation over Western Brazil/Eastern Peru, Argentina, central Africa, the Indonesia islands, and the coast of Burma. *Yuan et al.* [2013] examined CESM precipitation in comparison to precipitation derived from TRMM PR measurements and found that the model missed the nocturnal convective maximum over the Burma region. In addition, through examination of TRMM data, they found that stratiform precipitation makes up a larger percentage of total precipitation in this

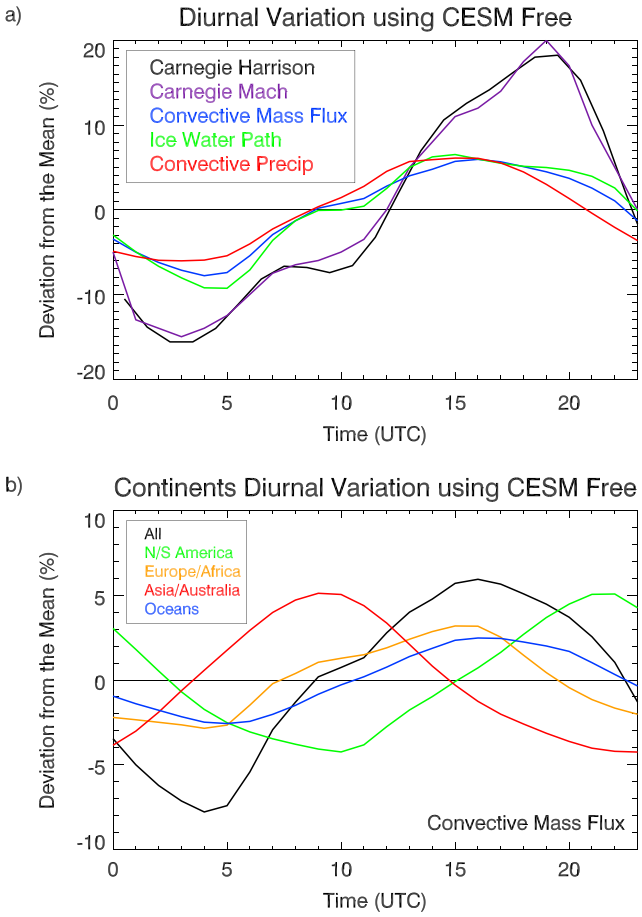

Figure 4. The *Harrison* [2013] Carnegie Curve (black) and the *Mach et al.* [2011] Carnegie Curve (purple) compared to the CESM free-running diurnal variations plotted as the percent deviation from the mean for (a) convective mass flux (blue), ice water path (green), and convective precipitation (red) and (b) convective mass flux for North and South America (green), Europe and Africa (orange), Asia and Australia (red), and the oceans (blue).

region. Since we are using convective precipitation, this likely contributes to the underestimation seen in this region. Specific causes of the biases seen in Brazil/Peru, Argentina, Africa, and Indonesia are uncertain at this time. However, these biases are known, and the Brazil/Peru region should be better represented in CESM version 2.0 (J. F. Lamarque, personal communication, 2016).

3.2. Diurnal Cycle Validation

When using current parameterizations based on model parameters in a full GEC model, capturing the observed diurnal variation of electrified cloud activity and strength is important. Therefore, the free-running and nudged CESM data were output hourly to examine the model representation of the diurnal cycle and compared with the Carnegie curve. The Carnegie curve is based on fair weather electric field measurements that were made on several cruises of the Carnegie and Maude ships throughout 2 years in the early 1900s and represents the diurnal variations of the electric potential gradient deviations from their mean. Given that electrified clouds play an important role in maintaining the potential difference between Earth's surface and the ionosphere, we would expect them to vary in phase with the Carnegie curve.

Figure 4a shows the free-running convective mass flux, ice water path, and convective precipitation totaled for each hour across 2005 and plotted as a deviation from the yearly mean. Comparing these images to the Carnegie curves in black and purple from *Harrison* [2013] and *Mach et al.* [2011], all three variables capture the general shape seen in the global diurnal cycle; however, the amplitude and timing differ slightly. RMS error values range between 6.6% for ice water path and 8.1% for convective precipitation, with 7.1% for convective mass flux. The Carnegie curve also shows a 15–20% variation about the mean, whereas output from CESM only varies by 5% to 8%, with convective precipitation showing the largest amplitude variation and ice water path the smallest. Furthermore, the minimum diurnal variation is 1 to 2 h late for convective mass flux and ice water path, but is generally accurate for convective precipitation. The maximum peak in the model diurnal cycle occurs 4 h early for convective mass flux and convective precipitation, and 6 h early for ice water path. Early initiation of convection is a known issue in CESM and other climate models, which tends to trigger convection too early and too frequently [*Dai and Trenberth*, 2004; *DeMott et al.*, 2007; *Gervais et al.*, 2014; *Folkins et al.*, 2014], as was discussed in section 3.1. This early initiation was also found in past GEC studies including *Mareev and Volodin* [2014].

Separating the model data into three chimney regions (Figure 4b) allows a more detailed look at the timing of convection across different regions. Specifically, we can compare our curves to the thunderstorm area seen in Figure 11 of *Harrison* [2013]. This image shows three distinct peaks; the Asia/Australia curve, which peaks at around 0800 UTC, shows the smallest amplitude, and is also the widest. The Africa/Europe curve in *Harrison*

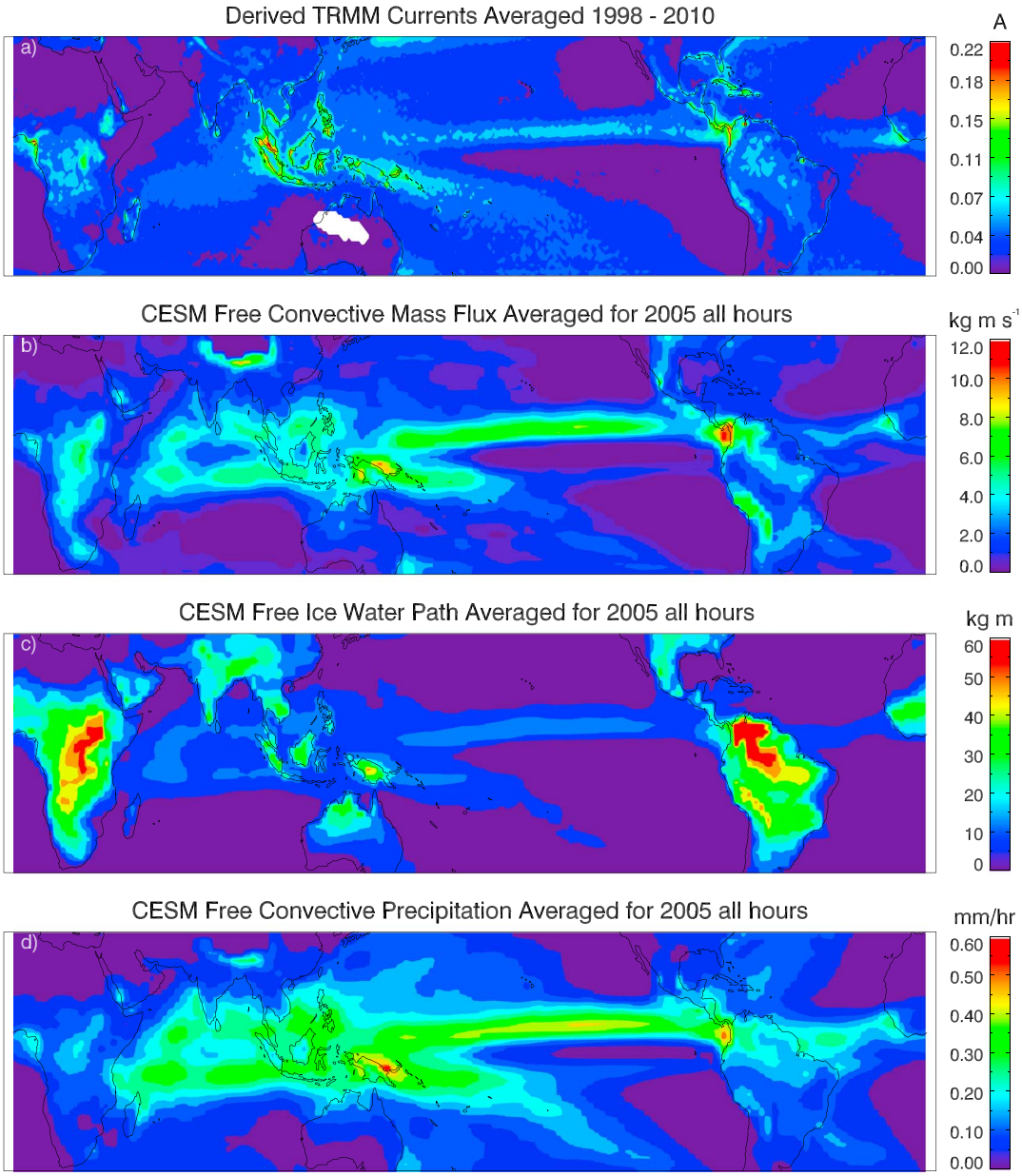

Figure 5. A comparison of the yearly (2005) averaged CESM free-running simulation variables to current derived from TRMM. The specific fields are (a) currents derived from the TRMM cloud and precipitation feature database, (b) convective mass flux, (c) ice water path, and (d) convective precipitation.

[2013] shows the largest and sharpest peak at around 1400 UTC, whereas the N/S America curve that peaks at 2000 UTC is sharper than the Asia/Australia curve and has an amplitude that is slightly less than the Africa/Europe curve.

In comparison to *Harrison* [2013] Figure 11, the model Asia/Australia chimney peak (Figure 4b) has too large a diurnal variation for all three different model parameters; it should be the smallest of the three chimney regions. The timing of the minimum matches well to that of the *Harrison* [2013] Asia/Australia minimum; however, the maximum peak timing is an hour late at 0900 UTC. The Africa/Europe chimney has the largest amplitude in *Harrison* [2013] but consistently shows the smallest diurnal variation in all three CESM variables. Also, the peak is much broader and flatter compared to *Harrison* [2013]. The minimum of all three CESM parameter diurnal variations occurs 1 to 3 h early, but the maximum is 2 h late at 1600 UTC in convective mass flux. For the North and South America chimneys, the widths of the curves match well to those presented in

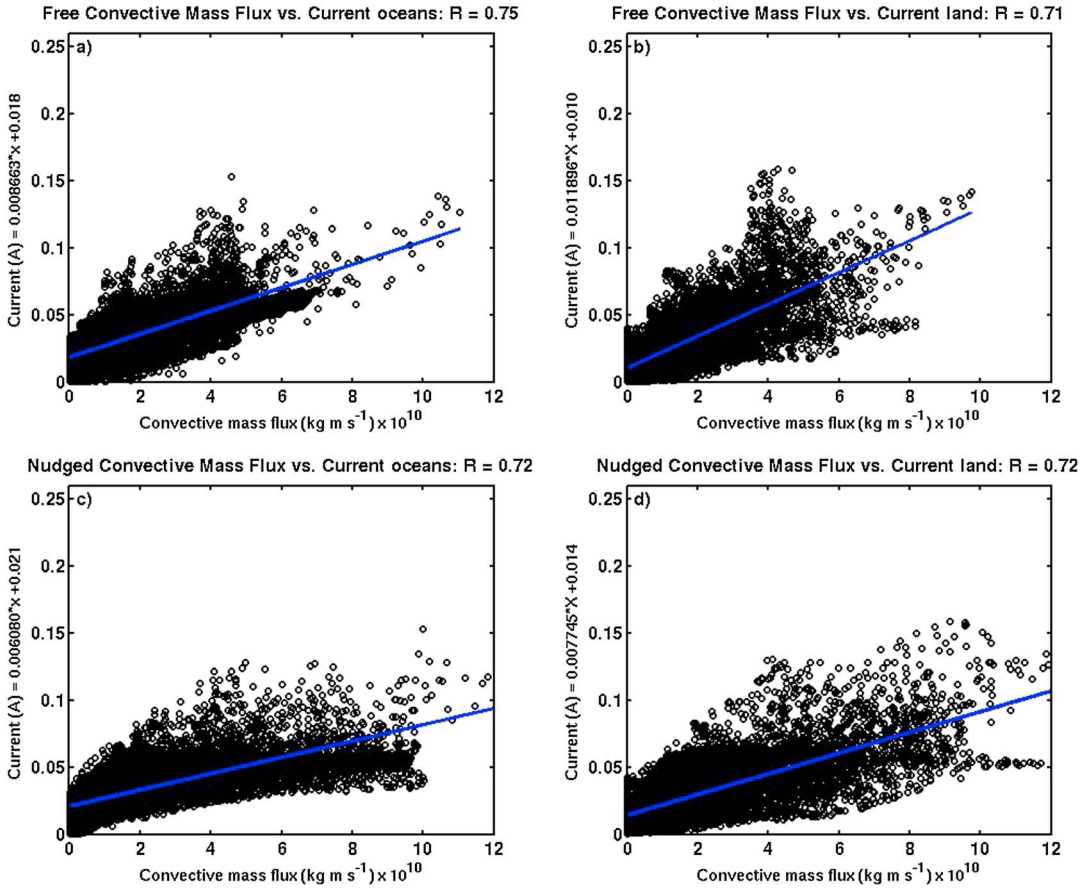

Figure 6. Averaged annual (2005) grid point by grid point values of CESM convective mass flux compared to TRMM-derived current from the (a) free-running oceans, (b) free-running land, (c) nudged oceans, and (d) nudged land.

Harrison [2013]. However, the curve minimum occurs 2 h early and the maximum occurs 2 h late at 2200 UTC for convective mass flux.

4. Development of Current Parameterizations in CESM

Although the model does show some regional biases, in general, it captures the timing and amplitude of convection. Therefore, the three model parameters are tested to determine whether they can be used to represent conduction currents. Convective mass flux, ice water path, and convective precipitation are compared to the derived currents (from section 2.3) on a grid point by grid point basis, as well as on averaged data. A parameterization is developed by fitting relationships to the grid point and averaged data comparisons.

Figure 5a shows the global distributions of these currents, while Figures 5b–5d show convective mass flux, ice water path, and convective precipitation averaged for 2005, respectively. All three variables capture many of the main features shown in the TRMM current approximations, including the ITCZ in the Pacific and Atlantic Oceans, and local maxima over Africa. However, the local maxima over Malaysia and the Philippines in the global current data are overrepresented by convective mass flux and convective precipitation. In addition, ice water path overestimates the maxima over Africa, and shifts the maxima over Costa Rica and Panama east of its actual location. All three variables show a local maximum over the Himalayas that is not represented in the TRMM-derived currents.

In comparison to the free-running simulation, the nudged run (not shown) displays less convective mass flux, ice water path, and convective precipitation over the ITCZ region, especially in the eastern Pacific. For

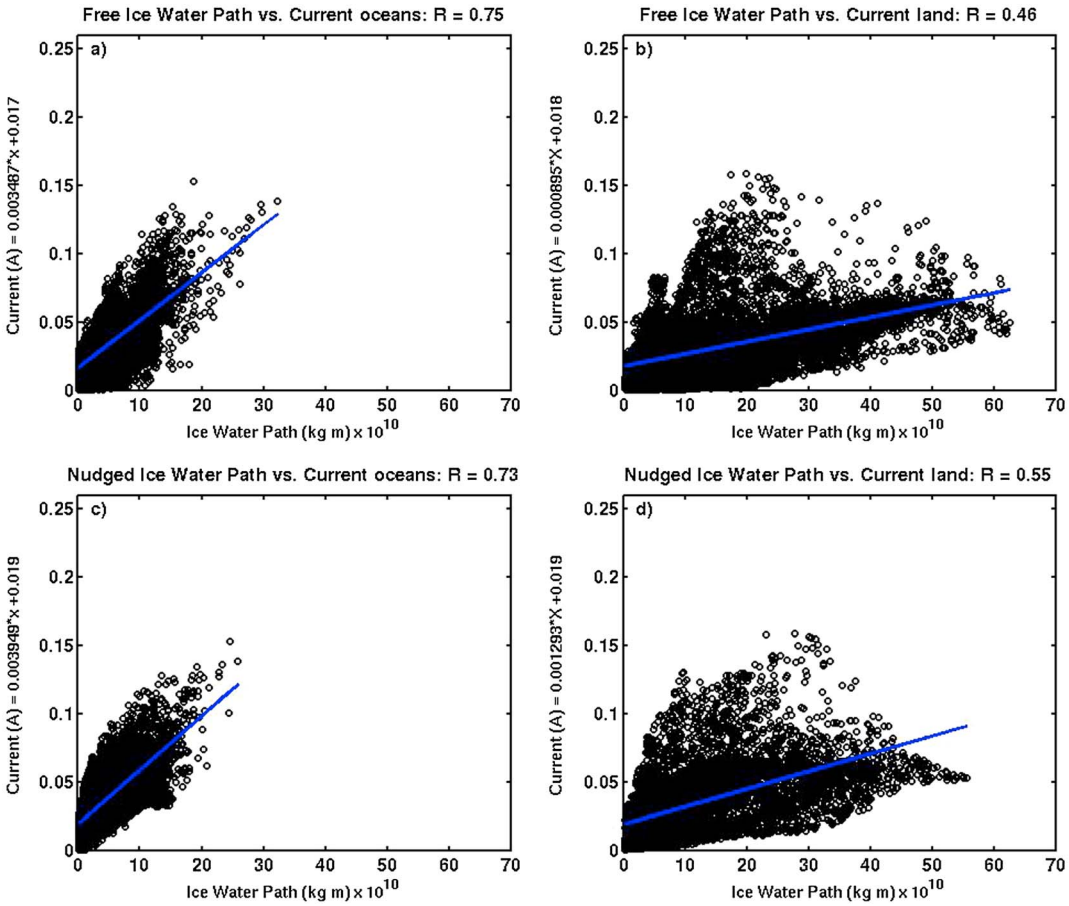

Figure 7. Averaged annual (2005) CESM ice water path compared to derived current from the (a) free-running oceans, (b) free-running land, (c) nudged oceans, and (d) nudged land.

convective mass flux, the local maxima near South America, north of Australia, and Africa are amplified. In contrast, ice water path shows a reduction in the intensity of the Africa and North/South America chimneys in the nudged model. Convective precipitation exhibits an increase off the coast of South America and over Africa. However, the region of larger convective precipitation over Malaysia is an expanded in area, but the peak value is reduced.

4.1. Regressions on Gridded Data

Linear regressions and the associated correlation coefficients were computed to investigate the relationship between CESM- and TRMM-derived currents. Figure 6 shows scatterplots of CESM free-running and nudged convective mass flux for 2005 against the derived total storm currents. The free-running ocean data exhibit the highest correlation coefficient at 0.77. The correlation coefficient is slightly less at 0.72 for the nudged land and ocean data, and lowest at 0.71 for the free-running land data. The nudged data show the largest convective mass fluxes, and all plots contain enhanced regions of scatter for currents above 0.2 A and convective mass fluxes above 3×10^{10} kg m s^{-1}. Linear regressions show a similar slope for the different regimes and model runs but are steepest for the free-running land data with a slope of 1.19×10^{8} kg m s^{-1} A^{-1} and shallowest for the nudged ocean data at 0.61×10^{8} kg m s^{-1} A^{-1}. The free-running ocean and nudged land data have similar slopes of 0.77×10^{8} and 0.87×10^{8} kg m s^{-1} A^{-1} respectively.

In comparison to convective mass flux, ice water path versus conduction currents (Figure 7) show increased scatter in the land regions, reflected by the lower correlation coefficients of 0.55 and 0.46. Correlation coefficients for the oceanic regions are similar to convective mass flux with values of 0.73 and 0.75 for the nudged and free-running versions, respectively. Ice water path demonstrates a strong regime dependence compared

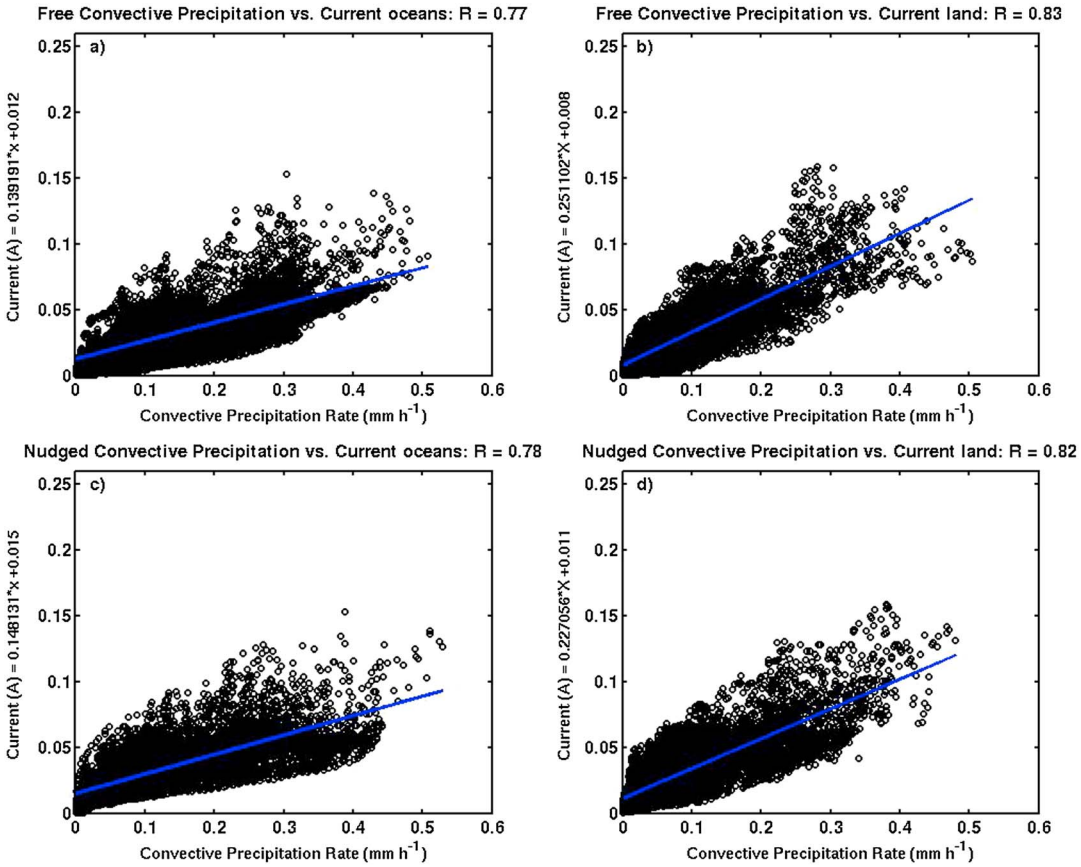

Figure 8. Averaged annual (2005) CESM convective precipitation compared to derived current from the (a) free-running oceans, (b) free-running land, (c) nudged oceans, and (d) nudged land.

to convective mass flux; the land regressions are flatter than their oceanic counterparts with slopes of 1.29×10^7 and 0.86×10^7 kg m A^{-1} for the nudged and free-running simulations versus 3.95×10^7 and 3.49×10^7 kg m A^{-1} for the oceans. The regime dependence suggests that storms over the oceans require a larger ice water path to produce the same currents that occur with a smaller ice water paths over land. This behavior is similar to TRMM-derived radar characteristics and lightning, which suggests that large ice particles occur more often over land than over oceans [*Liu et al.*, 2012]. Though oceanic storms exhibit less precipitation ice, current distributions from *Mach et al.* [2011] suggest that oceanic conduction currents have a larger mean than their continental counterpart, which results in larger conduction currents per ice water path for oceanic clouds.

Out of all three variables, convective precipitation from the free-running model simulation (Figure 8) has the highest correlation to conduction currents with a value of 0.83 over land. The free-running oceanic data, however, give correlation coefficients similar to convective mass flux and ice water path at 0.77. The nudged data yield very similar correlations to the free-running convective precipitation data at 0.82 and 0.78 for land and oceans, respectively. Convective precipitation displays a slight separation between land and oceans. This separation, however, is not as strong as that seen in the ice water path-current data. *Petersen et al.* [2005] suggested that the relationship between ice water path and lightning flash density was independent of convective regime. CESM does show different relationships for oceanic and land regimes but only for ice water path and convective precipitation. *Liu et al.* [2012] also indicated a regime dependence between land and oceans, with the largest slope for the land regimes, in agreement with CESM convective precipitation.

Convection over the oceans, especially the tropical oceans, tends to be dominated by warm rain processes. The combination of lower ice water path values and larger convective precipitation over the oceans, compared to the land data at the same currents, may suggest an increased contribution of warm rain processes to precipitation that does not contribute to the electrification of the storms in tropical oceanic convection [*Petersen and Rutledge*, 1998].

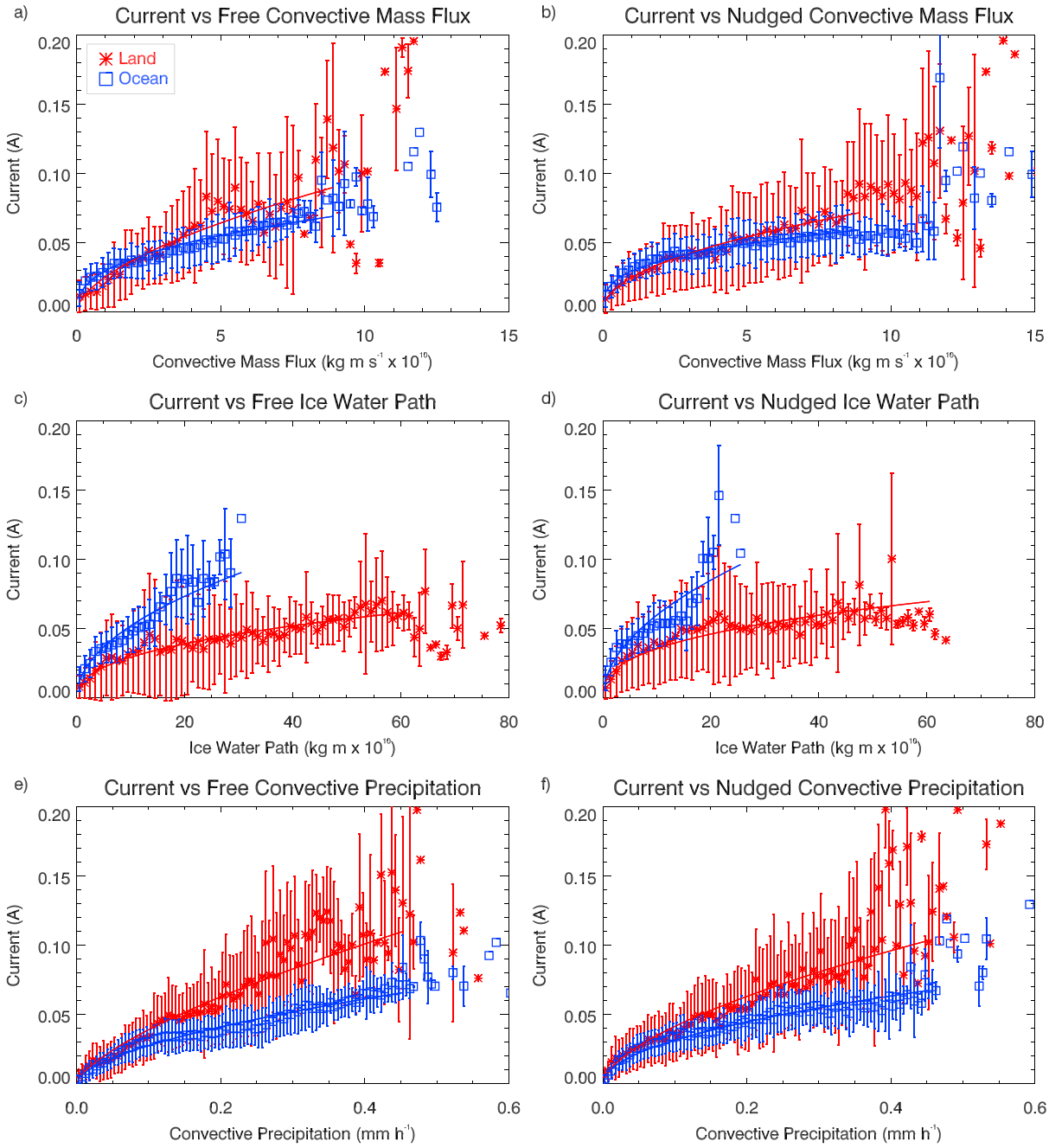

Figure 9. Yearly averaged (2005) CESM model output compared to derived current for (a) free-running convective mass flux, (b) nudged convective mass flux, (c) free-running ice water path, (d) nudged ice water path, (e) free-running convective precipitation, and (f) nudged convective precipitation. The symbols show the average value for each bin and the vertical lines represent 1 standard deviation away from the mean.

4.2. Regressions on Averaged Data

To further examine the relationship between conduction currents and the model parameters and also mitigate biases caused by large values associated with rare events, CESM convective mass flux, ice water path, and convective precipitation were binned and the mean current in each bin plotted as shown in Figure 9 for land (ocean) in red (blue). The bin sizes vary between parameters and are 0.2×10^{10} kg m s^{-1} for convective mass flux, 10^{10} kg m for ice water path, and 0.005 mm/h for convective precipitation. Vertical lines in Figure 9 show the range of data values in each bin, calculated as 1 standard deviation from the mean. Then, linear, logarithmic, power law, and polynomial fits were performed on this smoothed data to determine

Table 1. The Adjusted Goodness of Fits Calculated Over Land Areas for Convective Mass Flux, Ice Water Path, and Convective Precipitation From the Free-Running and Nudged CESM Simulations

	Land Adjusted Goodness of Fits (r^2)				
Variable	Linear	Logarithmic	Polynomial 3	Polynomial 4	Power
Form	$y = ax + b$	$y = a\ \ln(x) + b$	$y = ax^3 + bx^2 + cx + d$	$y = ax^4 + bx^3 + cx^2 + dx + e$	$y = ax^b$
Convective mass flux free	0.78	0.68	0.81	0.87	0.90
Convective mass flux nudged	0.94	0.80	0.95	0.95	0.97
Ice water path free	0.86	0.84	0.89	0.93	0.93
Ice water path nudged	0.56	0.73	0.70	0.76	0.84
Convective precipitation free	0.87	0.72	0.91	0.91	0.94
Convective precipitation nudged	0.83	0.59	0.87	0.87	0.93

the best relationship to represent conduction currents in the model. Table 1 shows a comparison of the coefficient of determination using these different relationships for the land convective mass flux, ice water path, and convective precipitation. The coefficient of determination is calculated by first introducing linearity to the data. Then,

$$r^2 = 1 - \frac{\mathrm{SSE}}{\mathrm{SSTO}}, \tag{5}$$

where $\mathrm{SSE} = \sum (Y_i - \hat{Y}_i)^2$, $\mathrm{SSTO} = \sum (Y_i - \hat{Y})^2$, Y_i is the sample data, $\overline{Y}$ the sample mean, and $\hat{Y}_i$ the fit data. To account for differing degrees of freedom, and adjusted coefficient of determination was calculated. The formula is given below as equation (6), where n is the total sample size and p is the number of predictors.

$$\text{adjusted}\, r^2 = 1 - \left(1 - r^2\right)\frac{n-1}{n-p} \tag{6}$$

Power law fits have the highest coefficient of determination as opposed to the linear and polynomial fits for data output from the free-running model simulations. They do not describe negative currents but are zero when the variable in question also has a value of zero. Therefore, we have employed a power law fit in the form of $y = ax^b$. Table 2 shows the coefficients a and b of the fits, and the adjusted r^2 value for all of the variables.

Figures 9a and 9b show the smoothed convective mass flux scatterplots compared to the computed current. In general, the fits between land and ocean are fairly similar, with the only difference being that the ocean fit is slightly flatter, as reflected by the smaller exponents. Similar to the original scatterplots (Figure 7), the nudged data contain larger convective mass fluxes than what can be observed in the free-running data. The adjusted coefficient of determination (r^2) is strong for the convective mass flux data, although slightly larger for the nudged land and ocean data at 0.97, compared to the free-running version at 0.90 and 0.94.

Consistent with fits derived from the grid point data, the smoothed ice water path (Figures 9c and 9d) versus currents show a strong separation between the ocean and land regimes, with the land fits being much flatter than the oceanic data, suggested by the larger exponents for the oceans. Also, there is no ocean ice water path data that exceed values of 30×10^{10} kg m^{-2}, and the free-running land data show the largest ice water path values. Adjusted goodness of fits are similar to those derived from the convective mass flux data with the free-running ice water path at 0.93 for land and 0.96 for oceans, and less for the nudged run at 0.84 and 0.86.

Table 2. The Power Law Fit Coefficients for Convective Mass Flux, Ice Water Path, and Convective Precipitation for the Free-Running and Nudged CESM Simulations

	Land			Ocean		
Variable	a	b	Adjusted r^2	a	b	Adjusted r^2
Convective mass flux free	0.03	0.58	0.90	0.03	0.39	0.94
Convective mass flux nudged	0.02	0.49	0.97	0.03	0.532	0.97
Ice water path free	0.01	0.42	0.93	0.20	0.50	0.95
Ice water path nudged	0.02	0.38	0.84	0.02	0.51	0.86
Convective precipitation free	0.19	0.69	0.94	0.10	0.59	0.98
Convective precipitation nudged	0.17	0.61	0.93	0.10	0.51	0.96

Comparing the smoothed convective precipitation data (Figures 9e and 9f) to the individual grid point data, some separation between the land and ocean regimes can be seen, but it is not as significant as the differences in ice water path. Relationships for the land data show more variability than those for the ocean data, especially at high precipitation rates. This is evidenced by the adjusted goodness of fit statistics which are slightly lower at 0.94 and 0.93 for the land free-running and nudged data, and larger for the ocean data with 0.98 and 0.96. Both land exponents are also larger than their oceanic counterparts at 0.69 and 0.61 for the nudged and free-running model simulations.

5. Model Parameterized Current Output

The regressions between convective mass flux, ice water path, convective precipitation and total conduction currents from the smoothed data sets were used to infer currents at each model grid point. Figure 10 shows the global distributions of derived currents from the free-running model simulations compared with derived currents from TRMM. Current derived from convective mass flux (Figure 10b) matches the major features of the TRMM currents seen in Figure 10a. However, the peak over Indonesia does not reach the same amplitude, and the aerial extent of the currents over the ITCZ, Indonesia, and Africa is too large. In addition, the maximum over the Himalayas is still evident in the derived currents, but not present in the TRMM currents. The global total value of 1452 A matches well to the estimate of 1400 A by *Kraakevik* [1961].

Similar to convective mass flux, ice water path-derived currents (Figure 10c) also capture the main features and produce too large an area of currents over the ITCZ, Indonesia, and Africa. In contrast, however, the maximum peak current derived from ice water path is smaller than that seen in convective mass flux, yet the global total current is larger at 1678 A. This is a result of the increased aerial extent of currents over the higher latitudes of the Atlantic and Pacific Oceans, likely associated with shower clouds. Ice water path does not show the distinct peaks, but rather the data is distributed more evenly, especially over South America.

Convective precipitation-inferred currents (Figure 10d) show the smallest total global current of 1136 A, in part because of the reduced currents found at the higher latitudes. This is likely a result of the increasing percentage of large-scale precipitation at these latitudes. The features in the tropics agree well with the total current map, including the maxima seen near the coast of Panama and over the Indonesian islands. Convective precipitation is highly correlated with currents over the tropics, as resolving convection accurately is the most important part for a correlation to the derived current data. However, correlations outside of the tropics may be more variable due to the above mentioned increasing percentage of large-scale precipitation.

Figure 11 shows the diurnal variations of current derived from CESM convective mass flux, ice water path, and convective precipitation. For convective mass flux and convective precipitation, the amplitude is similar to what was observed prior to the parameterization. However, RMS values are slightly larger, with 7.2% for convective mass flux, 8.6% for convective precipitation, and 10% for ice water path. Specifically, convective precipitation and convective mass flux show roughly a 6% variation about the mean, similar to the amplitude variation seen in Figure 4. Ice water path, however, shows the smallest variation about the mean at approximately 2%. Part of the reason why the ice water path diurnal variation is relatively too small is that the parameterization does not capture the extent of the variability of over land. This is indicated by the large amount of scatter in Figure 8 at currents above 0.05 A and the relatively large ice water path values seen over Africa and South America in Figure 5c. There are no comparable areas of large ice water path in Figure 10c.

Similar to the diurnal variations in Figure 4a, convective mass flux peaks 5 h early at 1500 UTC. The ice water path curve is much broader and flatter than the diurnal variations seen in Figure 4a and peaks even earlier at 1400 UTC. Convective precipitation also peaks far too early in the derived current version, with the maximum occurring at 1300 UTC and the minimum at 0300 UTC. The early maxima in all three curves are a direct result of the early initiation of convection, which is a known issue in CESM and other climate models, and was discussed in section 3.1.

Of the three variables, a convective mass flux parameterization captures the observed current sources best. The representation of the current source maxima in the tropics is superior to that seen for ice water path, though not as highly correlated as convective precipitation. However, convective precipitation shows the

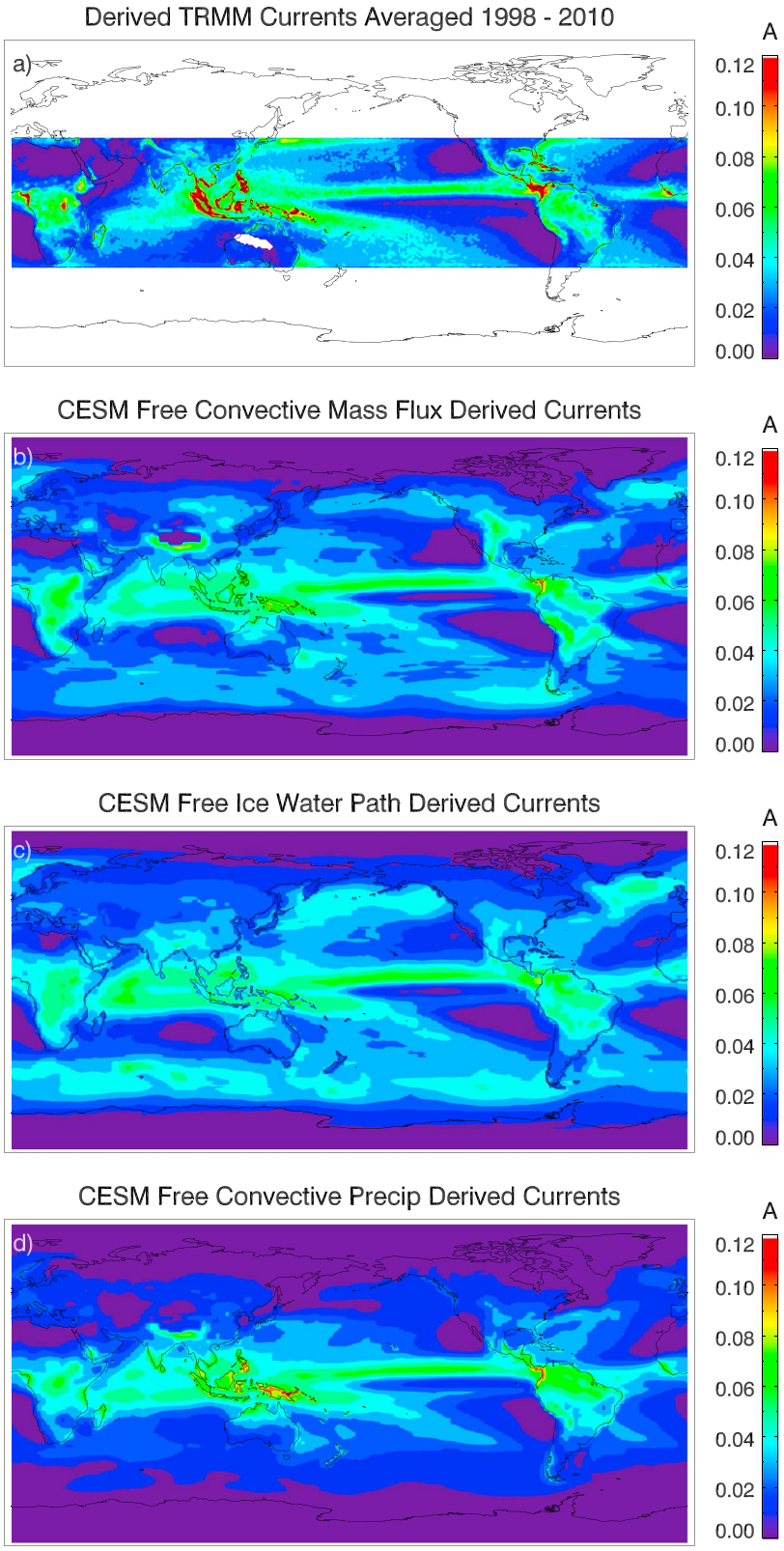

Figure 10. Derived current from (a) the TRMM precipitation and cloud database, (b) CESM free-running convective mass flux, (c) CESM free-running ice water path, and (d) CESM free-running convective precipitation.

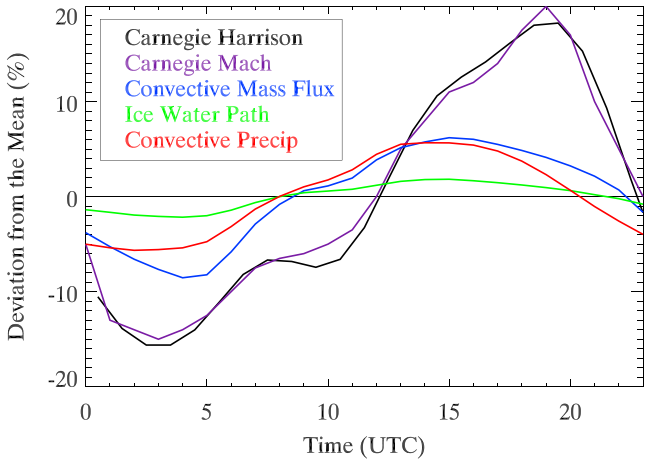

Figure 11. Derived current plotted as the percent deviation from the mean of CESM free-running convective mass flux (blue), ice water path (green), and convective precipitation (red) compared to the *Harrison* [2013] Carnegie Curve (black) and the *Mach et al.* [2011] Carnegie Curve (purple).

smallest global total and has reduced currents in the middle and high latitudes. Given that our observations are only for the tropical regions, there is uncertainty in whether convective precipitation is representative of the currents in this region. *Lucas et al.* [2015] used a more simplified version of the convective mass flux parameterization derived in this paper by computing the currents at each time step. They found that the modeled electric fields agreed well with observed diurnal variations over two Antarctic sites. However, they did note that the amplitude of the electric fields produced were too small, similar to what we find here.

6. Conclusions

Using model output from CESM, and precipitation feature data from TRMM, this study examines the model representation of currents derived from microphysical and dynamical properties of electrified clouds. These parameters have been previously shown to correlate well with cloud electrification and lightning. The goals of this study were to first determine the model skill at predicting these variables. Then, model parameterizations of conduction currents in the GEC were created and evaluated for use in a comprehensive global model.

The ability of model convective mass flux, ice water path, and convective precipitation to represent electrified cloud conduction currents was tested and evaluated. Annual global distributions of these parameters agree well with the geographical patterns of TRMM current estimates. On a grid point by grid point basis, convective mass flux shows a strong correlation to the TRMM-derived current data. The relationship between currents and convective mass flux is similar between land and ocean regions. In comparison, the ice water path and current relationships show a distinct difference between the land and ocean regions and considerably more scatter. Relationships between convective precipitation and currents do exhibit some regime dependence, but it is less distinct than that seen with ice water path.

Examining the diurnal cycle, the variations of convective mass flux, ice water path, and convective precipitation are fairly similar to electric potential variations represented by the Carnegie curve. However, the maximum occurs 4 to 6 h early in all three variables. In addition, the amplitude of these curves show a 5% to 8% variation about the mean, less than the Carnegie Curve's 15%.

Model biases are evident when the diurnal variations are separated into the three chimney regions. The model shows low biases of precipitation over South America, Africa, and regions of Asia. However, there is also a region of corresponding high bias over Asia and almost no bias over Australia. These biases likely contribute to the relatively large amplitude diurnal variation over Asia/Australia, whereas variations over Europe/Africa are too small. In addition, the Zhang McFarlane convection scheme likely contributes to the broader and flatter peak and smaller diurnal variation of the Europe/Africa curve by producing early initiation and smaller and more frequent storms. However, the local biases seen above are relatively small and do not impact the global total current values.

Current estimates produced from all three variables agree well to past studies, with the currents derived from the convective mass flux showing the best results. The main features of the ITCZ in the Pacific and Atlantic Oceans, and local maxima over Africa are captured well by all three variables. However, the output shows too small of a diurnal cycle, and overestimates currents over the Indian Ocean and Himalayas. In particular with continued improvements of the model representation of convection and electrified clouds in CESM, results herein suggest that using cloud parameters such as convective mass flux and to some extend ice

water path and convective precipitation are well suited for parameterizing currents in a global model framework. They are able to represent the global distribution and strength of current input for different electrified clouds.

However, there are a few limitations that are not considered in this study. First, validation data outside of the TRMM range (35°S to 35°N) would be needed to fully understand the impact of these biases. This is especially true in North America and Europe where convection frequently occurs north of 35° and is therefore missed by TRMM. Second, this study does not attempt to classify the type and size of clouds, as these are not resolved by the model. Instead, they are represented through bulk model parameters. Third, the two data sets which are used to create the observed current data show different amounts of ESCs. *Mach et al*. [2011] suggests that their work may underestimate the contribution of ESCs. When they increase the contribution of ESCs by 3 to 4 times, they get a better fit to the diurnal variation. This agrees well with *Liu et al*. [2010] who suggested the ratio of 3:1 for ESCs to thunderstorms. Both studies report that thunderstorms from land are the dominant source of current, though both of them have their own specific weaknesses in sampling. Further research is needed to resolve this discrepancy in the future.

Acknowledgments
This work was partly funded by the National Science Foundation Frontiers in Earth System Dynamics grant 1135446 and National Science Foundation grant 1519006. The National Center for Atmospheric Research is funded by the National Science Foundation. Data for this project can be accessed from the Research Applications Laboratory ftp site at ftp://ftp.rap.ucar.edu/pub/kalb/JGR_atmos.

References

Allen, D. J., and K. E. Pickering (2002), Evaluation of lightning flash rate parameterizations for use in a global chemical transport model, *J. Geophys. Res.*, *107*, 4711, doi:10.1029/2002JD002066.

Bailey, J. C., R. J. Blakeslee, and K. T. Driscoll (1999), Evidence for the absence of conductivity variations above thunderstorms, *NASA Conf. Publ.*, NASA/CP-1999-209261, 646-649.

Baumgaertner, A. J. G., G. M. Lucas, J. P. Thayer, and S. A. Mallios (2014), On the role of clouds in the fair weather part of the global electric circuit, *Atmos. Chem. Phys.*, *14*(16), 8599–8610, doi:10.5194/acp-14-8599-2014.

Bering, E. A., III, A. A. Few, and J. R. Benbrook (1998), The global electric circuit, *Phys. Today*, *51*, 24–32, doi:10.1063/1.882422.

Boccippio, D. J., S. J. Goodman, and S. Heckman (2000), Regional differences in tropical lightning distributions, *J. Appl. Meteorol.*, *39*, 2231–2248, doi:10.1175/1520-0450(2001)040<2231:RDITLD>2.0.CO;2.

Cecil, D. J., S. J. Goodman, D. J. Boccippio, E. J. Zipser, and S. W. Nesbitt (2005), Three years of TRMM precipitation features. Part I: Radar, radiometric, and lightning characteristics, *Mon. Weather Rev.*, *133*, 543–566, doi:10.1175/MWR-2876.1.

Cecil, D. J., D. E. Buechler, and R. J. Blakeslee (2014), Gridded lightning climatology from TRMM-LIS and OTD: Dataset description, *Atmos. Res.*, *135–136*, 404–414, doi:10.1016/j.atmosres.2012.06.028.

Christian, H. J., et al. (2003), Global frequency of lightning as observed from space by the optical transient detector, *J. Geophys. Res.*, *108*(D1), 4005, doi:10.1029/2002JD002347.

Dai, A., and K. E. Trenberth (2004), The diurnal cycle and its depiction in the Community Climate System Model, *J. Clim.*, *17*, 930–951, doi:10.1175/1520–0442(2004)017<0930:TDCAID>2.0.CO;2.

Dai, A., F. Giorgi, and K. E. Trenberth (1999), Observed and model-simulated diurnal cycles of precipitation over the contiguous United States, *J. Geophys. Res.*, *104*, 6377–6402, doi:10.1029/98JD02720.

Davydenko, S. S., T. C. Marshall, and M. Stolzenburg (2009), Modeling the electric structures of two thunderstorms and their contributions to the global electric circuit, *Atmos. Res.*, *91*, 165–177, doi:10.1016/j.atmosres.2008.08.006.

Deierling, W., W. A. Petersen, J. Latham, S. Ellis, and H. J. Christian (2008), The relationship between lightning activity and ice fluxes in thunderstorms, *J. Geophys. Res.*, *113*, D15210, doi:10.1029/2007JD009700.

Deierling, W., and W. A. Petersen (2008), Total lightning activity as an indicator of updraft characteristics, *J. Geophys. Res.*, *113*, D16210, doi:10.1029/2007JD009598.

DeMott, C. A., D. A. Randall, and M. Khairoutdinov (2007), Convective precipitation variability as a tool for general circulation model analysis, *J. Clim.*, *20*, 91, doi:10.1175/JCLI3991.1.

Dye, J. E., and J. C. Willett (2007), Observed enhancement of reflectivity and the electric field in long-lived Florida anvils, *Mon. Weather Rev.*, *135*, 3362–3380, doi:10.1175/MWR3484.1.

Folkins, I., T. Mitovski, and J. R. Pierce (2014), A simple way to improve the diurnal cycle in convective rainfall over land in climate models, *J. Geophys. Res: Atmospheres*, *119*, 2113–2130, doi:10.1002/2013JD020149.

Gervais, M., J. R. Gyakus, E. Atallah, B. Tremblay, and R. B. Neale (2014), How well are the distribution and extreme values of daily precipitation over North America represented in the Community Climate System Model? A comparison to reanalysis, satellite, and gridded station data, *J. Clim.*, *27*, 5219–5239, doi:10.1175/JCLI-D-13-00320.1.

Harrison, R. G. (2013), The Carnegie curve, *Surv. Geophys.*, *34*(2), 209–232, doi:10.1007/s10712-012-9210-2.

Heymsfield, G. M., J. B. Halverson, J. Simpson, L. Tian, and T. P. Bui (2001), ER-2 Doppler radar investigations of the eyewall of hurricane Bonnie during the Convection and Moisture Experiment-3, *J. Appl. Meteorol.*, *4-*, 1310–1330, doi:10.1175/1520-0450(2001)040<1310:EDRIOT>2.0.CO;2.

Jayaratne, E. R., C. P. R. Saunders, and J. Hallett (1983), Laboratory studies of the charging of soft hail during ice crystal interactions, *Q. J. R. Meteorol. Soc.*, *101*, 227–234, doi:10.1002/qj.49710946111.

Kalinin, A. V., E. A. Mareev, and A. A. Zhidkov (2011), Calculation of different-type clouds in the global atmospheric electric circuit, Proc. XIV Int. Conf. Atmos. Electr., Rio de Janeiro, Brazil.

Keith, W. D., and C. P. R. Saunders (1989), Charge transfer during multiple large ice crystal interactions with a riming target, *J. Geophys. Res.*, *94*, 13,103–13,106, doi:10.1029/JD094iD11p13103.

Kraakevik, J. H. (1961), Measurements of current density in the fair weather atmosphere, *J. Geophys. Res.*, *666*, 3735–3748, doi:10.1029/JZ066i011p03735.

Kuhlman, K. M., D. R. MacGorman, M. I. Biggerstaff, and P. R. Krehbiel (2009), Lightning initiation in the anvils of two supercell storms, *Geophys. Res. Lett.*, *36*, L07802, doi:10.1029/2008GL036650.

Kummerow, C., W. Barnes, T. Kozu, J. Shiue, and J. Simpson (1998), The Tropical Rainfall Measuring Mission (TRMM) sensor package, *Atmos. Oceanic Technol.*, *15*, 809–816, doi:10.1175/1520-0426(1998)015<0809:TTRMMT>2.0.CO;2.

Lang, T. J., S. A. Rutledge, J. E. Dye, M. Venticinque, P. Laroche, and E. Defer (2000), Anomalously low negative cloud-to-ground lightning flash rates in intense convective storms observed during TERAO-A, *Mon. Weather Rev.*, *128*, 160–173, doi:10.1175/1520-0493(2000)128<0160:ALNCTG>2.0.CO;2.

Latham, J. (1981), The electrification of thunderstorms, *Q. J. R. Meteorol. Soc.*, *17*, 277–298, doi:10.1002/qj.49710745202.

LeMone, M. A., and E. J. Zipser (1980), Cumulonimbus vertical velocity events in GATE. Part I: Diameter intensity and mass flux, *J. Atmos. Sci.*, *37*, 2444–2457, doi:10.1175/1520-0469(1980)037<2444:CVVEIG>2.0.CO;2.

Liu, C., E. Zipser, D. Cecil, S. W. Nesbitt, and S. Sherwood (2008), A cloud and precipitation feature database from 9 years of TRMM data, *J. Appl. Meteorol. Climatol.*, *47*, 2712–2728, doi:10.1175/2008JAMC1890.1.

Liu, C., E. R. Williams, E. Zipser, and G. Burns (2010), Diurnal variations of global thunderstorms and electrified shower clouds and their contribution to the global electrical circuit, *J. Atmos. Sci.*, *67*, 309–323, doi:10.1175/2009JAS3248.1.

Liu, C., D. J. Cecil, E. J. Zipser, K. Kronfeld, and R. Robertson (2012), Relationships between lightning flash rates and radar reflectivity vertical structures in thunderstorms over the tropics and subtropics, *J. Geophys. Res.*, *117*, D062121, doi:10.1029/2011JD017123.

Lucas, G. M., A. J. G. Baumgaertner, and J. P. Thayer (2015), A global electric circuit model within a community climate model, *J. Geophys. Res.*, *120*, 12,054–12,066, doi:10.1002/2015JD023562.

MacGorman, D. R., and W. D. Rust (1998), *The Electrical Nature of Storms*, 422 pp., Oxford Univ. Press, Okla.

Mach, D. M., R. J. Blakeslee, J. C. Bailey, W. M. Farrell, R. A. Goldberg, M. D. Desch, and J. G. Houser (2005), Lightning optical pulse statistics from storm overflights during the Altus Cumulus Electrification Study, *Atmos. Res.*, *76*, 386–401, doi:10.1016.j.atmosres.2004.11.039.

Mach, D. M., H. J. Christian, R. J. Blakeslee, D. J. Boccippio, S. J. Goodman, and W. L. Boeck (2007), Performance assessment of the optical transient detector and lightning imaging sensor, *J. Geophys. Res.*, *112*, D09210, doi:10.1029/2006JD007787.

Mach, D. M., R. J. Blakeslee, M. G. Batemann, and J. C. Bailey (2009), Electric fields, conductivity, and estimated currents from aircraft overflights of electrified clouds, *J. Geophys. Res.*, *114*, D10204, doi:10.1029/2008JD011495.

Mach, D. M., R. J. Blakeslee, M. G. Bateman, and J. C. Bailey (2010), Comparisons of total currents based on storm location, polarity, and flash rates derived from high-altitude aircraft overflights, *J. Geophys. Res.*, *115*, D03201, doi:10.1029/2009JD012240.

Mach, D. M., R. J. Blakeslee, and M. G. Bateman (2011), Global electric circuit implications of combined aircraft storm electric current measurements and satellite-based diurnal lightning statistics, *J. Geophys. Res.*, *116*, D05201, doi:10.1029/2010JD014462.

Mareev, E. A., and E. M. Volodin (2014), Variation of the global electric circuit and ionospheric potential in a general circulation model, *Geophys. Res. Lett.*, *41*, 9009–9016, doi:10.1002/2014GL062352.

Meneghini, R., J. A. Jones, T. Iguchi, K. Okamoto, and J. Kwiatkowski (2001), Statistical methods of estimating average rainfall over large space-timescales using data from the TRMM precipitation radar, *J. Appl. Meteorol.*, *40*, 568–585.

Mitchell, J. D., C. L. Croskey, S. P. Blood, C. Li, L. C. Hale, and R. A. Goldberg (1990), Middle atmosphere electrical structure during MAC/EPSILON, *J. Atmos. Terr. Phys.*, *52*, 1095–1104, doi:10.1016/0021-9169(90)90038-O.

Moore, D. S., and G. P. McCabe (1999), *Introduction to the Practice of Statistics*, W. H. Freeman and Company, New York.

Morrison, H., and A. Gettelman (2008), A new two-moment bulk stratiform cloud microphysics scheme in the community atmosphere model, version 3 (CAM3). Part I: Description and numerical tests, *J. Clim.*, *21*, 3642–3659, doi:10.1175/2008JCLI2105.1.

Morrison, H., J. A. Curry, and V. I. Khvorostyanov (2005), A new double-moment microphysics parameterization for application in cloud and climate models. part I: Description, *J. Atmos. Sci.*, *62*, 1665–1677, doi:10.1175/JAS3446.1.

Neale, R. B., et al. (2010), Description of the NCAR Community Atmosphere Model (CAM 5.0), NCAR Technical Note. [Available at http://www.cesm.ucar.edu/models/cesm1.0/cam/docs/description/cam5_desc.pdf.]

Neale, R. B., J. Richter, S. Park, P. H. Lauritzen, S. J. Vavrus, P. J. Rasch, and M. Zhang (2013), The mean climate of the Community Atmosphere Model (CAM4) in forced SST and fully coupled experiments, *J. Clim.*, *26*, 5150–5168, doi:10.1175/JCLI-D-12-00236.1.

Park, S., C. S. Bretherton, and P. J. Rasch (2014), Integrating cloud processes in the community atmosphere model, version 5, *J. Clim.*, *27*, 6821–6856, doi:10.1175/JCLI-D-14-00087.1.

Petersen, W. A., and S. A. Rutledge (1998), On the relationship between cloud-to-ground lightning and convective rainfall, *J. Geophys. Res.*, *103*, 14,025–14,040, doi:10.1029/97JD02064.

Petersen, W. A., H. J. Christian, and S. A. Rutledge (2005), TRMM observations of the global relationship between ice water content and lightning, *Geophys. Res. Lett.*, *32*, L14819, doi:10.1029/2005GL023236.

Price, C., and D. Rind (1992), A simple lightning parameterization for calculating global lightning distributions, *J. Geophys. Res.*, *97*(D9), 9919–9933, doi:10.1029/92JD00719.

Price, C., and D. Rind (1994), Possible implications of global climate change on global lightning distributions and frequencies, *J. Geophys. Res.*, *99*(D5), 10,823–10,831, doi:10.1029/94JD00019.

Raymond, D. J., and A. M. Blyth (1986), A stochastic mixing model for non-precipitating cumulus clouds, *J. Atmos. Sci.*, *43*, 2708–2718, doi:10.1175/1520-0469(1986)043<2708:ASMMFN>2.0.CO;2.

Raymond, D. J., and A. M. Blyth (1992), Extension of the stochastic mixing model to cumulonimbus clouds, *J. Atmos. Sci.*, *49*, 1968–1983, doi:10.1175/1520-0469(1992)049<1968:EOTSMM>2.0.CO;2.

Richter, J. H., and P. J. Rasch (2008), Effects of convective momentum transport on the atmospheric circulation in the Community Atmosphere Model version 3, *J. Clim.*, *21*(7), 1487–499, doi:10.1175/2007JCLI1789.1.

Rutledge, S. A., and W. A. Petersen (1994), Vertical radar reflectivity structure and cloud-to-ground lightning in the stratiform region of MCSs: Further evidence for in situ charging in the stratiform region, *Mon. Weather Rev.*, *122*, 1760–1776, doi:10.1175/1520-0493(1994)122<1760:VRRSAC>2.0.CO;2.

Saunders, C. P. R., and S. L. Peck (1998), Laboratory studies of the influence of the rime accretion rate on charge transfer during crystal/graupel collisions, *J. Geophys. Res.*, *103*, 13,949–13,956, doi:10.1029/97JD02644.

Shimizu, S., R. Oki, T. Tagawa, T. Iguchi, and M. Hirose (2009), Evaluation of the effects of the orbit boost of the TRMM satellite on PR rain estimates, *J. Meteorol. Soc. Jpn.*, *87A*, 83–92, doi:10.2151/jmsj.87A.83.

Stolzenburg, M., T. C. Marshall, W. D. Rust, and B. F. Smull (1994), Horizontal distribution of electrical and meteorological conditions across the stratiform region of a mesoscale convective system, *Mon. Weather Rev.*, *122*, 1777–1797, doi:10.1175/1520-0493(1994)122<1777:HDOEAM>2.0.CO.2.

Stolzenburg, M., W. D. Rust, and T. C. Marshall (1998), Electrical structure in thunderstorm convective regions: 3. Synthesis, *J. Geophys. Res.*, *103*, 14,097, doi:10.1029/97JD03545.

Stolzenburg, M., T. C. Marshall, W. D. Rust, and D. L. Bartels (2002), Two simultaneous charge structures in thunderstorm convection, *J. Geophys. Res.*, *107*, 4352, doi:10.1029/2001JD000904.

Sundqvist, H. (1988), Parameterization of condensation and associated clouds in models for weather prediction and general circulation simulation, in *Physically Based Modelling and Simulation of Climate and Climatic Change*, edited by M. E. Schlesinger, pp. 433–461, Kluwer, Dordrecht, Netherlands.

Takahashi, T., and K. Miyawaki (2002), Reexamination of riming electrification in a wind tunnel, *J. Atmos. Sci.*, *59*, 1018–1025, doi:10.1175/1520-0469(2002)059<1018:ROREIA>2.0.CO;2.

Tost, H., P. Jockel, and J. Lelieveld (2007), Lightning and convection parameterizations—Uncertainties in global modeling, *Atmos. Chem. Phys.*, *7*, 4553–4568.

Trenberth, K. E., A. Dai, R. M. Rasmussen, and D. B. Parsons (2003), The changing character of precipitation, *Bull. Am. Meteorol. Soc.*, *84*, 1205–1217, doi:10.1175/BAMS-84-9-1205.

Whipple, F. J. (1929), On the association of the diurnal variation of electric potential gradient in fine weather with the distribution of thunderstorms over the globe, *Q. J. R. Meteorol. Soc.*, *55*, 1–17.

Wiens, K. C., S. A. Rutledge, and S. A. Tessendorf (2005), The 29 June 2000 Supercell observed during STEPS. Part II: Lightning and charge structure, *J. Atmos. Sci.*, *62*(12), 4151–4177, doi:10.1175/JAS3615.1.

Williams, E. R., and E. Mareev (2014), Recent progress on the global electrical circuit, *Atmos. Res.*, *135–136*, 208–227, doi:10.1016/j.atmosres.2013.05.15.

Wilson, C. T. R. (1920), Investigations on lightning discharges and on the electric field of thunderstorms, *Philos. Trans. Roy. Soc. London*, *221A*, 73–115.

Yuan, W., R. Yu, M. Zhang, W. Lin, J. Li, and Y. Fu (2013), Diurnal cycle of summer precipitation over subtropical East Asia in CAM5, *J. Clim.*, *26*, 3159–3172, doi:10.1175/JCLI-D-12-00119.1.

Zhang, G. J., and N. A. McFarlane (1995), Sensitivity of climate simulations to the parameterization of cumulus convection in the Canadian Climate Centre general circulation model, *Atmosphere-Ocean*, *33*(3), 407–46, doi:10.1080/07055900.1995.9649539.

Zipser, E. J. (1994), Deep cumulonimbus cloud systems in the tropics with and without lightning, *Mon. Weather Rev.*, *122*, 1837–1851, doi:10.1175/1520-0493(1994)122<1837:DCCSIT>2.0.CO;2.

Zipser, E. J., and M. A. LeMone (1980), Cumulonimbus vertical velocity events in GATE. Part II: Synthesis and model core structure, *J. Atmos. Sci.*, *37*, 2458–2469, doi:10.1175/1520-0469(1980)037<2458:CVVEIG>2.0.CO;2.

Zipser, E. J., and K. Lutz (1994), The vertical profile of radar reflectivity of convective cells: A strong indicator of storm intensity and lightning probability?, *Mon. Weather Rev.*, *122*, 1751–1759, doi:10.1175/1520-0493(1994)122<1751:TVPORR>2.0.CO;2.